Primary intrinsic defects and their charge transition levels in β-Ga_2O_3

C. Zimmermann,* V. Rønning, Y. Kalmann Frodason, V. Bobal, and L. Vines
Physics Department/Centre for Materials Science and Nanotechnology, University of Oslo, P. O. Box 1048, Blindern, Oslo N-0316, Norway

J. B. Varley
Lawrence Livermore National Laboratory, Livermore, California 94550, USA

(Received 10 December 2019; revised 30 April 2020; accepted 23 June 2020; published 24 July 2020)

A steady-state photocapacitance (SSPC) setup directly connected to the beamline of a MeV ion implanter is utilized to study primary intrinsic defects in β-Ga_2O_3 generated by He implantation at cryogenic temperatures (120 K). At low temperatures, the migration of defects is suppressed, and hence the generation of primary intrinsic defects is expected to prevail. SSPC measurements reveal defect-related optical transitions in halide vapor-phase epitaxy (HVPE) -grown β-Ga_2O_3 thin films with onset energies at 1.3 (T_1), 1.7 (T_2), 1.9 (T_3), 2.6 (T_4), 3.7 (T_5), and 4.2 eV (T_6). T_2, T_4, T_5, and T_6 were observed in as-received HVPE-grown β-Ga_2O_3 thin films, whereby T_2 is only sporadically observed. The introduction rates for T_3, T_4, as well as T_6 indicate an origin related to primary intrinsic defects. Notably, T_1 and T_3 are only observed after He implantation at cryogenic temperatures. Hybrid-functional calculations were performed to estimate the optical absorption cross-section spectra for the gallium (Ga_i) and oxygen (O_i) interstitials as well as the corresponding vacancies (V_{Ga} and V_O, respectively), and compared with the measured onsets for optical absorption found by SSPC measurements. Indeed, we propose T_3 to be associated with $Ga_i^{(+/+2)}$ and/or $V_{GaI}^{(-3/-2)}$, while T_4 is suggested to be related to $V_{OK}^{(0/+)}$ (K = I, II, III) and/or $V_{GaII}^{(-3/-2)}$. Additionally, several further charge-state transition levels associated with V_{GaI} and V_{GaII} may contribute to T_4 and T_6. We further studied the kinetics of the defects created with He implantation by exposing the sample to room temperature. The kinetics observed for T_3 and T_4 further support the proposed assignments of the corresponding defect signatures.

DOI: 10.1103/PhysRevMaterials.4.074605

I. INTRODUCTION

Beta gallium oxide (Ga_2O_3) is a wide-band-gap semiconductor exhibiting exceptionally high breakdown electrical fields [1], and hence it has attracted considerable attention in recent years as a potential candidate for applications in UV sensors and power electronics [1–4]. Intrinsic as well as extrinsic defects have a profound influence on the optical and electrical properties of the material. For example, defects can act as recombination centers limiting the efficiency of UV sensors, or as traps for charge carriers and affect the performance of devices for power electronics [4–7]. Thus, understanding prominent defects in Ga_2O_3 is of the utmost importance in enabling the material to live up to its potential.

First-principles defect calculations predict several electronic states within the band gap of Ga_2O_3 associated with the primary intrinsic defects [8–19]. Gallium vacancies (V_{Ga}) are expected to be deep acceptors, the gallium interstitial (Ga_i) is associated with donor states, the oxygen vacancies (V_O) give rise to deep donor states, and the oxygen interstitial (O_i) can be either a donor or an acceptor depending on its configuration [15–17,19]. Notably, V_O and V_{Ga} can occur in different configurations [15–17,19].

Experimentally, a multitude of electronic states within the band gap of Ga_2O_3 have so far been unveiled using deep-level transient spectroscopy (DLTS) [15,20–26], deep-level optical spectroscopy (DLOS) [26–28], steady-state photocapacitance (SSPC) measurements [22,23,25–30], as well as a variety of other methods [23–25,29,31–35]. For example, SSPC studies performed by Farzana *et al.* as well as Zhang *et al.* on Ga_2O_3 reveal electronic states inside the Ga_2O_3 band gap at around 2.2, 3.2, and 4.4 eV below the conduction-band edge (E_C) [26–28], while at least six defect levels have been identified in the upper part of the band gap by DLTS [15,20,21,24–26]. Identifying the microscopic origin of the observed defect signatures, however, remains challenging, and hence only a few assignments have been made so far. One notable exception is the case of Fe_{Ga}, which was shown to introduce an electronic state at around 0.78 eV below E_C and identified by DLTS [21]. The electronic levels associated with intrinsic defects and their complexes, however, have so far escaped experimental identification.

One approach to studying intrinsic defects in semiconductors is by intentionally introducing such defects via irradiation or implantation using neutrons, protons, α-particles, electrons, or heavier ions [15,23,28,36,37]. Ga_i and O_i are, however, expected to be very mobile at, or even below, room temperature [14,15,38]. Furthermore, one can expect impurities, like hydrogen, to have a low migration barrier, and hence they are likely to passivate or form complexes with (intrinsic) defects. Notably, it has been implied by simulations as well as experimental studies that, for example, hydrogen and V_{Ga} can form complexes [19,39].

*christian.zimmermann@fys.uio.no

 ©2020 American Physical Society

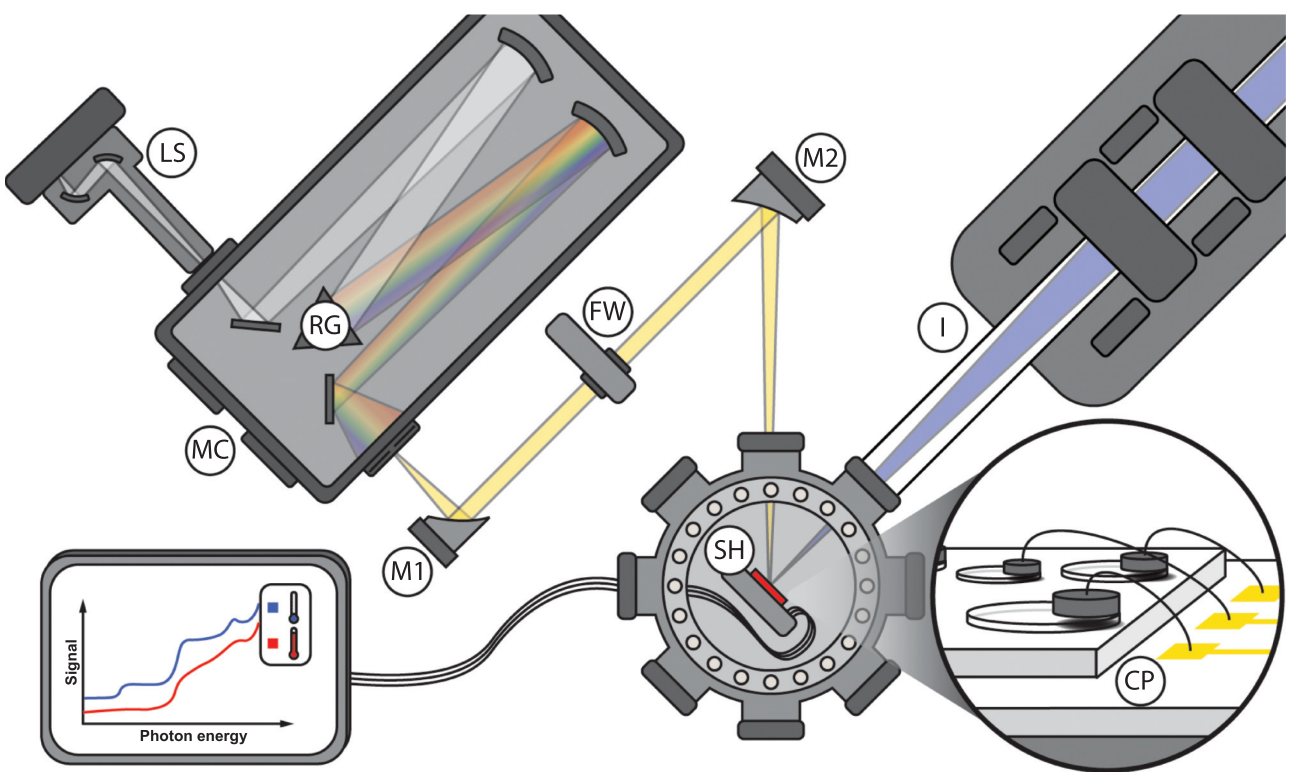

FIG. 1. Overview of the setup used for on-line SSPC measurements. The optical excitation at variable wavelength is provided by a white light source (LS) dispersed by a monochromator (MC) utilizing a grating (RG). The near-monochromatic light is steered toward the sample (SH) using parabolic mirrors (M1 and M2). Long-pass filters (FW) are used to suppress artifacts due to second-order diffraction. The sample (SH) is placed inside a cryostat that is directly connected to the beam line of a MeV ion implanter (I), and hence SSPC measurements can be performed on-line. The inset shows the contact layout: Semitransparent contacts are electrically connected by wire-bonding to minimize shadowing for light as well as for ions.

At sufficiently low temperatures, however, primary intrinsic defects as well as impurities are immobile, and hence the formation of primary intrinsic defects should prevail during low-temperature irradiation or implantation. This can be utilized by combining low-temperature irradiation or implantation with characterization at the beamline of an accelerator (on-line), i.e., irradiation at cryogenic temperatures and subsequent characterization without heating up the sample [40,41]. Moreover, subsequent exposure of the sample to higher temperatures can shed light on the defect kinetics in the corresponding temperature range, potentially revealing defect complex formation or passivation of defects.

In this work, we present results from on-line SSPC measurements on Ga_2O_3 thin films grown by halide vapor-phase epitaxy implanted with He at 120 K. Our measurements reveal several new defect signatures that we propose to be associated with primary intrinsic defects. In particular, Ga_i and/or V_{Ga} formed on a tetrahedral Ga site (V_{GaI}) are potential candidates for a level with an onset for optical absorption at around 1.9 eV. We further propose that V_O- and other V_{Ga}-related defects show optical absorption in the region of 2.5–3.7 eV. These results are further corroborated by hybrid-functional calculations estimating the optical absorption expected for Ga_i and V_{Ga} and V_O. Additionally, our results indicate that passivation and/or migration of such defects indeed occurs already at temperatures below room temperature.

II. METHODOLOGY

A. Experimental details

The Ga_2O_3 thin films studied here were grown by halide vapor-phase epitaxy (HVPE) on conductive Ga_2O_3 substrates and obtained from Novel Crystal Technology, Inc. [4]. The thin films are unintentionally doped with Si and exhibit nominal charge-carrier concentrations in the range of 5×10^{16}–3×10^{17} cm^{-3}. The thickness of the thin films is around 10 μm, while their surface corresponds to the (001) plane. Using a laser cutter, the as-obtained wafers were cut into pieces measuring approximately 5×5 mm^2. The sample pieces were subsequently cleaned with acetone, isopropanol, and deionized water for 5 min each inside an ultrasonic bath. Afterward, Ohmic backside contacts consisting of Ti (thickness = 10 nm) and Al (thickness = 150 nm) were deposited by e-beam evaporation. After a subsequent cleaning step, semitransparent Ni (thickness = 20 nm) Schottky contacts were deposited by e-beam evaporation using a shadow mask with contact diameters of 300, 600, and 900 μm. To ensure mechanical stability of the Ni contacts for wire-bonding, a second deposition of Ni (thickness = 150 nm) was performed using a shadow mask (with only circular openings displaying a diameter of 300 μm), which aligned with the semitransparent Ni contacts. The contact layout is shown in the inset of Fig. 1. All results shown here were obtained on semitransparent contacts with a diameter of 600 μm. Wire-bonding on the thick part of the

Ni contact was used for connecting the sample to electrical measurement instruments.

He ions were implanted at 120 K with an energy of 180 keV and fluences Φ ranging from 1.25×10^{11} to 5×10^{11} cm^{-2}. Negligible heating of the sample during He implantation is expected due to the utilization of low ion currents as well as low ion fluences. The defect generation was simulated utilizing Monte Carlo simulations implemented within the The Stopping and Range of Ions in Matter (SRIM) package [42] using displacement energies for Ga and O of 25 and 28 eV, respectively. Simulations were run for Ni thicknesses of 20 nm (semitransparent region) and 170 nm (thick Ni region used for wire-bonding), resulting in projected ranges R_p of 400 nm for a Ni thickness of 170 nm, and 610 nm for a Ni thickness of 20 nm, respectively. Notably, during He implantation primary intrinsic defects are generated regardless of their formation energy in thermal equilibrium [42]. After generation, these primary intrinsic defects may form energetically more favorable configurations if they are mobile enough at the sample temperature to relax into the corresponding configurations.

Current-voltage (IV) and capacitance-voltage (CV) measurements were carried out under dark conditions at room temperature as well as at 120 K using a Keithley 6487 picoammeter/voltage source and a Boonton 7200 capacitance meter, respectively. CV measurements were performed at a probing frequency f_probe of 1 MHz. A relative static dielectric constant ε_s of 10.2 was assumed for $\mathrm{Ga_2O_3}$ [43]. CV and IV measurements were performed inside a closed-cycle He cryostat connected to the beamline of an MeV ion implanter. From the forward bias region of IV curves, we extracted the ideality factor of the investigated Schottky junctions in order to verify the suitability of the junctions for SSPC measurements [44].

SSPC measurements were conducted utilizing the same closed-cycle He cryostat connected to the beamline of an MeV ion implanter (on-line) as was used for IV and CV measurements. Figure 1 shows the layout of the experimental setup used for on-line SSPC measurements. For studying defect kinetics, subsequent heat treatments up to room temperature were performed inside the same cryostat without transferring the sample. During SSPC measurements, the capacitance of the junction is recorded after illuminating the junction at a certain wavelength λ or photon energy E for a given time. A constant angle of incidence was used for illumination. Here, the photocapacitance was recorded after 5 min using a Boonton 7200 capacitance meter ($f_\mathrm{probe} = 1$ MHz) while the junction was kept at a fixed external bias (typically between -8 and -1 V). A laser-driven light source (EQ-77 from Energetiq) was used as a white light source, covering the spectral range from 190 to 2500 nm. The unpolarized light was dispersed with a grating-based monochromator (Shamrock 500i from ANDOR). Utilizing a grating with 1200 lines/mm (blaze at 400 nm) as well as fully opened exit and entrance slits at 2.5 mm, a typical spectral resolution of $\sim$20 meV was obtained. Long-pass filters were used to ensure that no light from second-order diffraction reaches the sample. Typical photon fluxes of 1×10^{17} $\mathrm{m^{-2}\,s^{-1}}$ in the UV and 1×10^{19} $\mathrm{m^{-2}\,s^{-1}}$ in the visible part of the spectrum were estimated using a calibrated thermal power meter placed at the sample position inside the cryostat. The near-monochromatic light was delivered to the sample using parabolic mirrors. The sample was illuminated starting at the long-wavelength end (usually at around 1600 nm), proceeding to shorter wavelengths in steps of 20 or 40 meV. In contrast to other studies, no filling pulse or above-band-gap illumination was utilized during SSPC measurements (see, for example, Refs. [28,44]). Samples were, however, preilluminated for 30 min at the longest wavelength used for a specific measurement range. This ensures that at the beginning of the measurement, traps responding to longer wavelengths than the ones used for the SSPC measurement are being ionized, and hence the sample is in or close to a steady state for illumination at such wavelengths. For some samples, the preillumination is not sufficient to reach comparable conditions as were encountered for measurement ranges involving longer wavelengths. For these samples, small discontinuities are seen close to the spectral positions where long-pass filter changes occurred. These discontinuities can be regarded as experimental artifacts.

The resulting photocapacitance signal is accumulative and represents the persistent charge created within the depletion region of the Schottky diode upon illumination at a certain photon energy. SSPC spectra recorded using different measurement ranges usually displayed slight offsets compared to each other. Offsets caused by switching between different measurement ranges were corrected assuming them to be independent of photon energy and using the measurement range for the lowest photon energies as reference.

SSPC spectra $S(E)$ are usually presented as

$$S(E) = 2\frac{C_\mathrm{illumination}(E) - C_\mathrm{dark}}{C_\mathrm{dark}} N_\mathrm{D} = 2\frac{\Delta C_\mathrm{illumination}(E)}{C_\mathrm{dark}} N_\mathrm{D}. \quad (1)$$

Here, E is the photon energy and $C_\mathrm{illumination}(E)$ denotes the (photo)capacitance due to illumination at a certain photon energy E. C_dark represents the capacitance measured at a fixed reverse bias prior to illumination, and hence $\Delta C_\mathrm{illumination}(E)$ denotes the change in capacitance due to illumination. N_D represents the donor concentration. Each electronic state inside the band gap will give rise to a steplike feature in SSPC spectra, and hence SSPC spectra can be represented by the following empirically motivated model:

$$S(E) = 2N_\mathrm{D} \sum_i \frac{\Delta C_\mathrm{illumination,i}}{C_\mathrm{dark}} \frac{1}{1 + \exp\left(-\frac{E - E_\mathrm{i}}{\gamma_\mathrm{i}}\right)}, \quad (2)$$

where the individual contributions i are described by sigmoidal functions. $\Delta C_\mathrm{illumination,i}/C_\mathrm{dark}$ represents the relative change in capacitance due to illumination for an individual contribution and is independent of E. For a specific contribution i, E_i describes the position of the onset of the SSPC signal and γ represents the steepness of the corresponding step. Features with $\Delta C_\mathrm{illumination,i}/C_\mathrm{dark} > 0$ (optically induced electron emission) as well as $\Delta C_\mathrm{illumination,i}/C_\mathrm{dark} < 0$ (optically induced hole emission) can occur [26–28,44,45]. SSPC spectra can also be represented as derivatives with respect to photon energy [45,46], where steplike features are transformed into peaklike features. Such a representation can greatly improve the interpretation of the technique, and aid deconvolution [46,47].

The height $2N_\mathrm{D}\Delta C_\mathrm{illumination,i}/C_\mathrm{dark}$ of each step is related to the effective trap concentration $N_\mathrm{t,i}^\mathrm{eff}$ and serves as a lower

bound for the actual concentration $N_{t,i}$ [45]. For small total trap concentrations N_t or $\Delta C_{illumination}/C_{dark} \ll 0.5$, a linear relationship holds between $\Delta C_{illumination,i}/C_{dark}$ and $N_{t,i}^{eff}$:

$$N_{t,i}^{eff} = 2\frac{\Delta C_{illumination,i}}{C_{dark}} N_D \frac{W^2}{W^2 - x_1^2}. \quad (3)$$

Here, W is the depletion layer width. x_1 denotes the depth where the electronic state of the trap level associated with contribution i crosses the Fermi level E_F. For determining x_1, one needs to know the thermodynamic charge transition level for a specific defect. This level can be estimated from E_i [see Eq. (2)] by assuming a value for the Franck-Condon shift d_{FC} [48,49]. The term $W^2/(W^2 - x_1^2)$ is often called λ-correction [44].

For larger total trap concentrations N_t or $\Delta C_{illumination}/C_{dark} \approx 0.5$, Eq. (3) does not hold and the trap concentrations can be estimated from $\Delta C_{illumination,i}/C_{dark}$ by numerically solving the steady-state capacitance under illumination for $N_{t,i}^{eff}$. More information about how to extract $N_{t,i}^{eff}$ in the case of low and large total trap concentrations can be found in the Supplemental Material [50].

Notably, all defects inside the space-charge region with a thermodynamic charge-state transition level below the Fermi level will contribute to the measured SSPC signal $S(E)$. Moreover, the value determined for $N_{t,i}^{eff}$ will depend on the competition between optically induced hole and electron emission for the trap i [44,45] as well as the mobility of electrons and holes (see the Supplemental Material [50]).

B. Computational details

First-principles calculations were performed using the projector augmented wave method (PAW) [51,52] and the Heyd-Scuseria-Ernzerhof screened hybrid functional (HSE) [53], as implemented in the VASP code [54]. The fraction of screened Hartree-Fock exchange was adjusted to $\alpha = 0.32$, which accurately describes both the experimental band gap ($E_g = 4.9$ eV) and structural parameters as reported elsewhere [21,55,56]. The experimentally determined band-gap value can be expected to exhibit an uncertainty of around ± 0.1 eV [55]. The Ga $3d$ and Ti $3p$, $3d$, as well as $4s$ electrons were included as valence states. For defect calculations, we used 160-atom supercells, a plane-wave energy cutoff of 400 eV, and a single special k-point at (1/4, 1/4, 1/4). Defect formation energies and thermodynamic charge-state transition levels were calculated by following the well-established formalism [57]. For charged defects, we adopted the anisotropic [58] Freysoldt, Neugebauer, and Van de Walle scheme to correct formation energies [59], and the method recently proposed by Gake *et al.* to correct vertical transition energies [60]. Optical absorption energies of defects were estimated by using the effective one-dimensional configuration coordinate (CC) model with parameters obtained from the HSE calculations [49,59]. However, the absorption onset will be lower than the classical absorption energy E_{abs} obtained from CC diagrams due to vibrational broadening. Absorption cross sections that include vibrational broadening can be simulated based on CC diagrams by following the scheme outlined in Refs. [49,61].

Following Refs. [49,61], defect-related optical absorption is modeled as an electronic transition between a ground state (defect in charge state q and charge carrier localized at or close to the defect) and an excited state (defect in charge state $q \pm 1$ and delocalized charge carrier in the conduction or valence band) triggered by a photon. Despite the complex optical selection rules in Ga_2O_3 due to the crystal symmetry and orbital character of the conduction and valence bands [55,56,62,63], the corresponding optical transitions are assumed to be allowed. Notably, defect-related optical transitions can be expected to be allowed if the transition is accompanied by strong lattice relaxation [64], which has been reported for various defects in Ga_2O_3 [19]. Moreover, the defect potential is assumed to be represented by a δ-function, in accordance with what is typically assumed for deep-level defects [61,65]. The excited state is a continuum of states in the conduction or valence band, whereby the bands are assumed to be parabolic. We note that we focus on transitions to the conduction band around E_C, which is a highly dispersive state that is predominantly parabolic and exhibits a simpler orbital character than the upper valence bands [55,56,62,63]. For the determination of the onset of defect-related optical absorption, the parabolic approximation is not believed to introduce a large error. Furthermore, the transition matrix element relevant for the electronic transition is assumed to be constant, i.e., to be independent of energy or momentum. The model proposed by Alkauskas *et al.* [49] and Kopylov *et al.* [61] takes phonon contributions into account: (i) phonons are emitted during the absorption process, and (ii) ground and excited states possess vibrational substates that will be occupied at higher temperatures and contribute to the optical absorption. It is assumed that the phonon contributions can be modeled by using an effective frequency for the phonons relevant for the ground and excited state, respectively. Notably, both (i) and (ii) will contribute to a broadening of the defect-related optical absorption cross-section spectra and a corresponding shift of the absorption onset. Phonon emission (i) will contribute to the broadening already at 0 K, whereas the contribution of additional vibrational substates (ii) will become more pronounced with increasing temperature. The calculations presented in this work were performed at 0 K. For a selection of defects, optical absorption cross-section spectra were also calculated assuming 120 K, and we found only minor differences. More information regarding the model used for calculating defect-related optical absorption cross-section spectra and their temperature dependence can be found in the Supplemental Material [50].

Migration barriers were evaluated using the climbing nudged elastic band method (cNEB) [66], using at least five images and requiring the resulting force to be $\leqslant 0.03$ eV Å^{-1}. Due to their large computational cost, barriers were evaluated using the same supercell geometries and the PBEsol functional [67] and PAW potentials that treated the Ga $3d$ electrons in the core. The lowest barriers were evaluated with HSE using the same approach to assess the differences.

III. RESULTS

A. Computational results

Hybrid-functional calculations were performed to predict optical signatures originating from various primary intrinsic

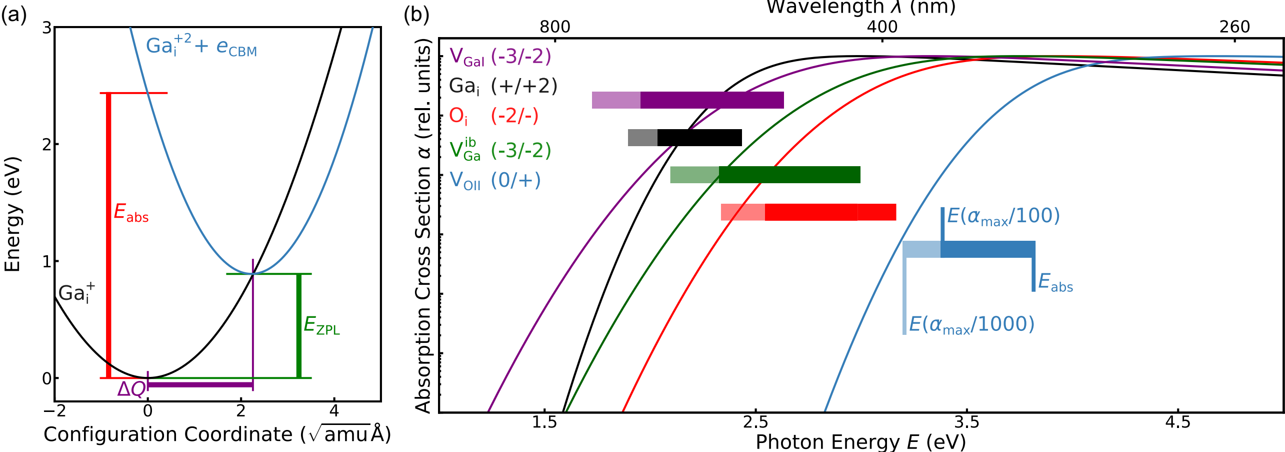

FIG. 2. (a) CC diagram for the (+/+2) charge-state transition of Ga_i. The vertical transition energy connected to optical absorption is marked as E_{abs}, while the thermodynamic transition level is marked as E_{ZPL}. The minima of the parabola signify the (meta)stable configurations of Ga_i^+ and Ga_i^{+2}, respectively. The corresponding difference in the configuration coordinate ΔQ is also marked in the plot. The values for E_{abs}, E_{ZPL}, and ΔQ for $Ga_i^{(+/+2)}$ as well as various other primary intrinsic defects and some defect complexes involving intrinsic defects are summarized in Table I. (b) Absorption cross-section spectra calculated for charge-state transitions of various primary intrinsic defects. The bars represent the interval defined by E_{abs} [as defined in (a)] and $E(\alpha_{max}/1000)$ for the corresponding transition. The position of $E(\alpha_{max}/100)$ is also indicated. $E(\alpha_{max}/1000)$ marks the photon energy at which the absorption cross section decreased by three orders of magnitude as compared to α_{max}, whereas $E(\alpha_{max}/100)$ marks the photon energy at which the absorption cross section decreased by two orders of magnitude as compared to α_{max}.

defects in Ga_2O_3. Specifically, we computed CC diagrams to obtain optical absorption spectra related to charge-state transitions associated with the primary intrinsic defects. For each defect, we focused on the charge-state transition with the energetically lowest transition energy associated with optical absorption. However, it can be expected that some primary intrinsic defects will exhibit more than one charge-state transition level inside the band gap of Ga_2O_3 [15]. Moreover, we only considered charge-state transitions involving the defects and the conduction band (optically induced electron emission). Due to the likely formation of self-trapped holes in Ga_2O_3 [68,69], we assume transitions between the defects and the valence band to not significantly contribute to the measured SSPC spectra (see the Supplemental Material [50]). Calculations were performed for Ga_i, O_i, V_{OK} (K = I, II, III), and V_{GaJ} (J = I, II). V_{GaJ} (J = I, II) was shown previously to prefer significantly relaxed configurations labeled as V_{Ga}^{iM} ($M = a, c, b$) [15]. The energy barrier for V_{GaJ} (J = I, II) to transform into V_{Ga}^{iM} ($M = a, c, b$) is predicted to be around 0.5–0.7 eV [15,19]. Optical signatures related to absorption were also calculated for V_{Ga}^{iM} ($M = a, c, b$). V_{OK} (K = I, II, III), V_{GaJ} (J = I,II), and V_{Ga}^{iM} ($M = a, c, b$) are defined according to Refs. [15,16]. V_{OI} and V_{OII} have a threefold symmetry, while V_{OIII} exhibits a fourfold symmetry. V_{GaI} is a gallium vacancy on a tetrahedral gallium site, while V_{GaII} denotes a gallium vacancy on an octahedral site. V_{Ga}^{iM} ($M = a, b, c$) are relaxed configurations, essentially consisting of a Ga atom moving into the gallium vacancy. V_{Ga}^{iM} can be viewed as a Ga interstitial with two neighboring Ga half-vacancies [19]. Graphical representations of the calculated structures can be found in the Supplemental Material [50]. Additionally, optical signatures related to absorption were also computed for a selection of favorable defect complexes consisting of V_O and V_{Ga} (divacancy complexes) [15]. A thorough study of defect complexes is, however, beyond the scope of this work.

Figure 2(a) shows a CC diagram computed for the charge-state transition from + to +2 for Ga_i. From the CC diagrams, E_{abs}, E_{ZPL}, and ΔQ can be determined. E_{abs} is the classical absorption energy, while E_{ZPL} is the energy of the zero-phonon line, which describes the thermodynamic charge transition level. ΔQ is the difference in configuration coordinate between the different charge states of the defect. The parameters E_{abs}, E_{ZPL}, and ΔQ are summarized in Table I for various primary intrinsic defects and some divacancy complexes. Typically, the difference between E_{abs} and E_{ZPL}, and hence the Franck-Condon shift d_{FC}, is in the range of 0.8–1.7 eV. This suggests that the charge-state transitions involve a large lattice relaxation. In contrast, significantly lower Franck-Condon shifts were estimated so far experimentally for defects in Ga_2O_3 [26–28]. More computational results regarding optical absorption spectra related to primary intrinsic defects can be found in the Supplemental Material [50].

Computed normalized absorption cross-section spectra (α) are shown in Fig. 2(b) for various primary intrinsic defects. An interval was extracted from these spectra covering all photon energies from E_{abs} [as defined in Fig. 2(a)] to $E(\alpha_{max}/1000)$, while the position of $E(\alpha_{max}/100)$ is also indicated. Hereby, α_{max} denotes the maximum value of the absorption cross-section spectra. $E(\alpha_{max}/1000)$ is defined as the photon energy where α decreased by three orders of magnitude as compared to α_{max}, whereas $E(\alpha_{max}/100)$ is defined as the photon energy where α decreased by two orders of magnitude as compared to α_{max}. These intervals are used for comparison between computational results and measured SSPC spectra.

To gauge the kinetics of primary intrinsic defects, migration barriers E_m were calculated for Ga_i, while results for

TABLE I. Summary of parameters for various primary intrinsic defects and some divacancy complexes obtained from hybrid-functional calculations. Calculations were performed for the charge-state transition associated with the energetically lowest transition energy associated with optical absorption. Hereby, only charge-state transitions involving the defects and the conduction band were considered. The parameters E_{ZPL}, E_{abs}, and ΔQ are obtained from CC diagrams and defined in Fig. 2(a). $E(\alpha_{max}/1000)$ is defined as the photon energy at which the absorption cross section decreased by three orders of magnitude as compared to α_{max}, whereas $E(\alpha_{max}/100)$ denotes the photon energy at which the absorption cross section decreased by two orders of magnitude as compared to α_{max}.

Defect	Charge state transition	ΔQ ($\sqrt{\text{amu}}$ Å)	E_{ZPL} (eV)	E_{abs} (eV)	$E(\frac{\alpha_{max}}{100})$ (eV)	$E(\frac{\alpha_{max}}{1000})$ (eV)
Ga_i	(+/+2)	2.22	0.89	2.43	2.04	1.90
O_i	(−2/−)	4.33	1.45	3.16	2.55	2.34
V_{OI}	(0/+)	3.85	1.68	3.20	2.79	2.63
V_{OII}	(0/+)	3.26	2.46	3.82	3.38	3.20
V_{OIII}	(0/+)	3.30	1.67	3.00	2.60	2.45
V_{GaI}	(−3/−2)	2.38	1.80	2.63	1.96	1.73
V_{GaII}	(−3/−2)	3.12	2.35	3.21	2.62	2.40
V_{Ga}^{ia}	(−3/−2)	2.24	2.16	3.06	2.42	2.19
V_{Ga}^{ib}	(−3/−2)	2.35	2.02	2.99	2.33	2.10
V_{Ga}^{ic}	(−3/−2)	2.37	2.65	3.48	2.82	2.59
V_{Ga}^{ic}-V_{OIII}	(−1/0)	2.40	3.04	4.16	3.62	3.42
V_{Ga}^{ib}-V_{OI}	(−1/0)	2.32	2.41	3.61	3.06	2.85
V_{GaII}-V_{OII}	(−3/−2)	3.10	1.60	2.55	1.93	1.71

E_m are already available for O_i, V_O, and V_{Ga} in the literature [14,15,38]. For O_i, a value of 0.12 eV was calculated for E_m [15]. For V_O, values from 1.2 to 4 eV were found, while for V_{Ga} barriers between 0.5 and 2.3 eV were computed [14]. Notably, the migration of V_{GaJ} (J = I, II) is associated with the formation of the configurations V_{Ga}^{iM} ($M = a, c, b$) [19]. However, the barrier for the V_{Ga}^{iM} ($M = a, c, b$) configurations to migrate or transform back into V_{GaJ} (J = I, II) are significantly higher [19]. For Ga_i, we find that the lower bound for E_m is strongly dependent on the charge state of Ga_i. We find an E_m of 0.65 eV for Ga_i^+, and we compute a barrier of 0.48 eV for Ga_i^{3+}. It is found that Ga_i^{2+} is metastable and will transform immediately into Ga_i^{3+}, meaning Ga_i exhibits so-called negative-U behavior [48]. Larger migration barriers were obtained when performing the calculations using the HSE functional, and hence the migration barriers stated above can be seen as lower bounds. More information regarding these calculations can be found in the Supplemental Material [50].

Following the approach of Kyrtsos *et al.*, a lower temperature can be estimated at which migration of defects will occur [14]. For V_O, Kyrtsos *et al.* estimate that such defects will not be mobile at or below room temperature, while for V_{Ga} some migration might occur already just below room temperature [14]. Notably, this migration is connected to the transformation of V_{GaJ} (J = I, II) into V_{Ga}^{iM} ($M = a, c, b$) [19]. However, the V_{Ga}^{iM} ($M = a, c, b$) configurations are less mobile than V_{GaJ} (J = I, II) and are not expected to migrate at or below room temperature [19]. For Ga_i, we can estimate that Ga_i^{3+} will be mobile at around 190 K, while Ga_i^+ will be mobile at around 250 K. O_i is expected to be mobile already at around 50 K given its low migration barrier of 0.12 eV [15]. Note also that electrical fields as they are present within a space-charge region may enhance the diffusion of charged defect species [14,70].

B. Experimental results

Figure 3(a) shows IV curves recorded on a Ni/Ga_2O_3/Ti/Al junction comprising a HVPE-grown Ga_2O_3 thin film. The junction displays a high rectification of around eight orders of magnitude. The investigated junctions generally display rectifications ranging from three to nine orders of magnitude. The series resistances range from several Ω to a few hundred Ω depending on the specific junction. The ideality factor at room temperature is typically around 1–1.5, but increases to values of around 3–4 for measurements at 120 K. After He implantation, all diodes exhibit an increase in series resistance, while usually no significant change in the reverse bias region is observed.

In Fig. 3(b), the results of typical CV measurements are displayed for one particular junction [same junction as depicted in Fig. 3(a)]. The donor concentration N_D for all diodes investigated is in the range of 2×10^{16}–2×10^{17} cm^{-3}, whereby the donor profiles generally show a slight decrease in donor concentration toward the surface. We estimate the uncertainty for N_D to be around 10% due to uncertainties in the contact area and the value of ε_s [43,71]. The typical probing depth is in the range of 300–700 nm, i.e., the main part of the region where implantation-induced defects are to be expected is within the probing volume. The conductance does not exceed 20 mS. After He implantation, N_D decreases, resulting in a probing depth of approximately 450–700 nm.

In the following, we will describe the results obtained from SSPC measurements performed at 120 K. Figure 4 displays a SSPC spectrum recorded on an as-received HVPE-grown Ga_2O_3 thin film. Steps in the SSPC spectrum can be seen with onset energies at 1.7, 2.6, 3.7, 4.2, and 4.8 eV. The corresponding defect signatures are labeled as T_2 (1.7 eV), T_4 (2.6 eV), T_5 (3.7 eV), and T_6 (4.2 eV), while the signature at 4.8 eV is associated with the band gap and is labeled as E_g in Fig. 4. T_5 is also associated with a decreasing SSPC signal starting at a photon energy of around 3.9 eV. The trap concentrations $N_{t,i}^{eff}$ are estimated to be in the range of 1×10^{14} cm^{-3}–1×10^{16} cm^{-3} using Eq. (3). The low defect concentrations confirm that all defect-related photoexcitation processes can be regarded as independent of each other. The detection limit for the sample shown in Fig. 4 is estimated to be around 1×10^{13} cm^{-3}. Notably, SSPC spectra recorded on various other as-received HVPE-grown Ga_2O_3 thin films exhibit the same features with the exception of T_2, which is only sporadically observed.

Figure 4 also displays a comparison between SSPC spectra recorded at 120 K before and after He implantation performed at 120 K with a fluence Φ of 1.25×10^{11} cm^{-2}. Two new signatures with onset energies at around 1.3 and 1.9 eV appear after He implantation. The corresponding signatures were labeled T_1 and T_3, respectively. T_1 does not appear in all samples subjected to He implantation, while T_3 is detected

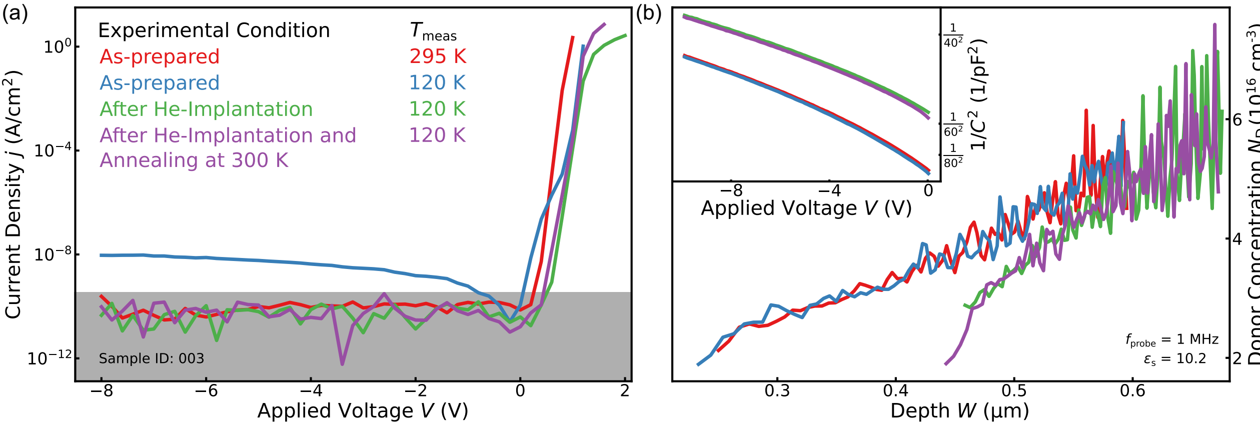

FIG. 3. (a) Results of IV measurements performed on a $Ni/Ga_2O_3/Ti/Al$ junction comprising a HVPE-grown Ga_2O_3 thin film. Measurements were conducted at 120 K and at room temperature for the as-prepared junction. After He implantation at 120 K as well as after a subsequent heat treatment at room temperature, additional IV measurements were performed. Both these measurements were conducted at 120 K. The junction displays a high rectification of around eight orders of magnitude. The ideality factor is in the range of 1.5–4. No pronounced changes besides an increase in series resistance can be seen in the IV characteristics after He implantation. (b) Results of CV measurements performed on the same junction and for the same experimental conditions as stated in (a). Donor concentration profiles derived from the CV measurements are displayed. The inset shows $1/C^2$ vs V plots for the same measurements. The donor concentration is in the order of 4×10^{16} cm^{-3}. After He implantation, a decrease in donor concentration can be seen, especially toward the surface of the Ga_2O_3 thin film.

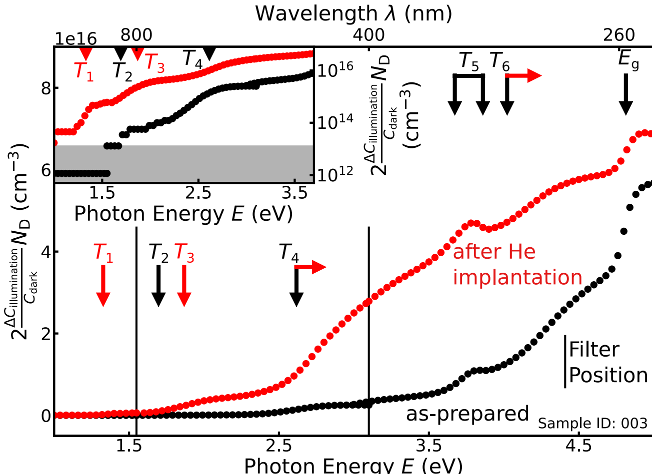

FIG. 4. SSPC spectra recorded on a HVPE-grown Ga_2O_3 thin film before and after implantation with He ions at 120 K. The He ions were implanted with a fluence of 1.25×10^{11} cm^{-2}. The photon energy positions of the low-pass filters are indicated with black vertical lines. Several defect signatures are observed before He implantation and marked with black vertical arrows as well as labeled T_2, T_4, T_5, and T_6. T_5 displays an increasing as well as decreasing signal. Furthermore, a signal that can be attributed to the band gap E_g is detected. After He implantation, new features marked with vertical red arrows and labeled T_1 and T_3 are observed. The defect signatures T_4 and T_6 change in amplitude and exhibit a shift of onset position (marked with a horizontal red arrow). The inset shows a logarithmic representation of the same data for lower photon energies. In this representation, the features T_1–T_3 can be seen more clearly. The estimated detection limit for SSPC measurements is shown as a grey area in the inset and equals a trap concentration of around 1×10^{13} cm^{-3} [estimated using Eq. (3)].

in all samples after He implantation conducted at 120 K. The features labeled T_4 and T_6 exhibit an apparent shift of their onset position after He implantation (marked with horizontal red arrows in Fig. 4). Furthermore, T_4 shows an increase in amplitude, while the apparent amplitude of T_6 decreases. There seems to be no significant impact of the He implantation on T_5. Finally, the influence of He implantation on the signature labeled T_2 is challenging to determine due to its low concentration and sporadic presence.

In Fig. 5(a), SSPC spectra are shown that were recorded on a HVPE-grown Ga_2O_3 thin film. SSPC spectra are displayed for the as-received thin film as well as for the thin film after implantation with He ions with different fluences at 120 K. The sample was subjected to two subsequent He implantations, and hence two different accumulated fluences Φ_{tot}. Derivative SSPC spectra are displayed for comparison in the top panel of Fig. 5(a). The derivative SSPC spectra suggest the presence of several overlapping defect signatures contributing to T_4 and T_6, which is supported by modeling the spectra (see the Supplemental Material [50]). Notably, the comparison of the derivative SSPC spectra recorded before and after He implantation at 120 K indicates that the subfeatures being part of T_4 and T_6 respond slightly differently to He implantation.

Vertical bars are displayed in Fig. 5(a) to indicate the energetic positions of the optical absorption associated with various primary intrinsic defects as predicted by computations based on hybrid functionals [see Fig. 2(b)]. Indeed, the prediction for the optical absorption related to $Ga_i^{(+/+2)}$ and $V_{GaI}^{(-3/-2)}$ overlaps with T_3, while the optical absorption related to $O_i^{(-2/-)}$, $V_{OK}^{(0/+)}$ (K = I, II, III), and $V_{GaII}^{(-3/-2)}$ overlaps with T_4. Note, however, that the onset of optical absorption will depend on the absolute value of the absorption cross section,

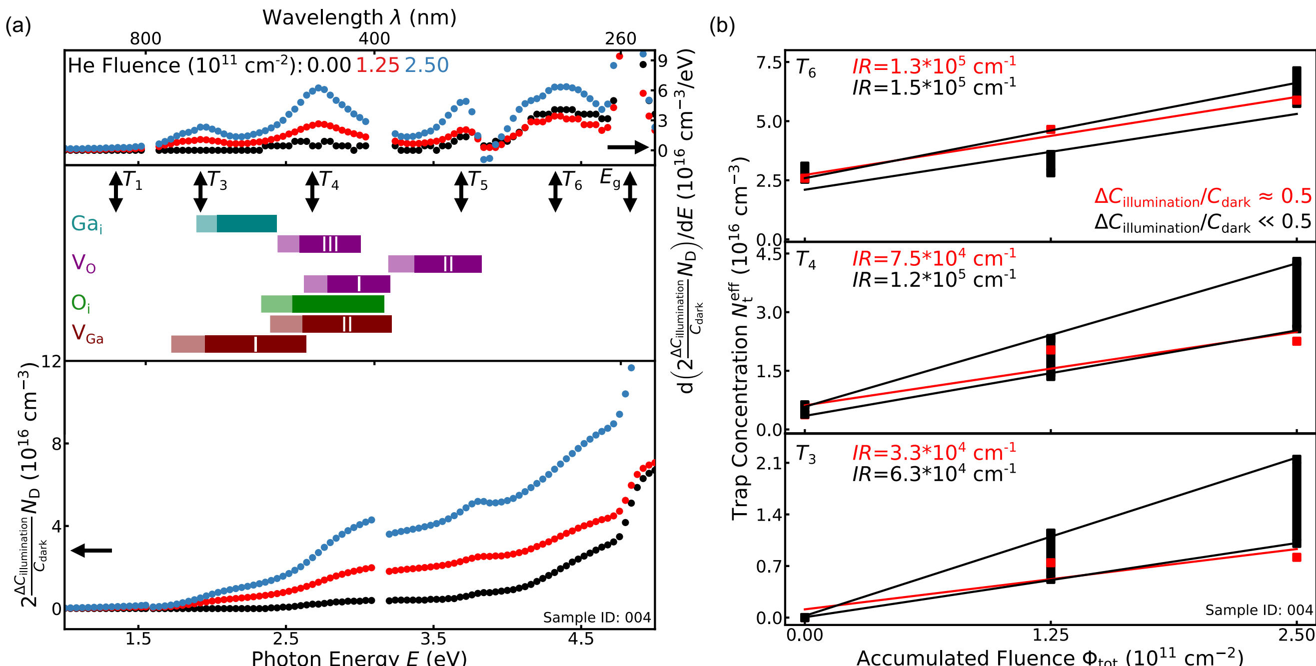

FIG. 5. (a) Results of SSPC measurements recorded on a HVPE-grown Ga_2O_3 thin film before and after subsequent implantations with He ions at 120 K. The results are displayed as derivative SSPC spectra (upper panel) and as conventional SSPC spectra (lower panel). The legend states the accumulated implantation fluence Φ_{tot} for the corresponding data set. The onset positions observed in the SSPC spectra are marked with black vertical arrows. The defect signature labeled T_2 (see Fig. 4) was not detected in this sample. From the width and shape of the derivative SSPC spectra, it can be inferred that, especially, T_4 and T_6 consist of several overlapping features. Upon He implantation, T_3 is created, while T_4 as well as T_6 change in concentration. The vertical bars indicate where computations based on hybrid functionals predict the optical absorption of the primary intrinsic defects to occur (see Fig. 2). I, II, and III denote the different configurations found for V_O and V_{Ga} in Ga_2O_3. (b) Plot of the effective trap concentration $N_{t,i}^{eff}$ derived for the features labeled T_3, T_4, and T_6 in dependence of the accumulated He fluence Φ_{tot}. $N_{t,i}^{eff}$ was calculated for the case of $\Delta C_{illumination}/C_{dark} \ll 0.5$ [see Eq. (3)] and $\Delta C_{illumination}/C_{dark} \approx 0.5$ (see the Supplemental Material [50]). For $\Delta C_{illumination}/C_{dark} \ll 0.5$, the corresponding data points cover values computed for the case of neglecting the λ-correction as well as for assuming a Franck-Condon shift d_{FC} of 1 eV (see the Supplemental Material [50]). The effective trap concentrations $N_{t,i}^{eff}$ associated with T_6, T_4, and T_3 display a linear dependence with accumulated He fluence Φ_{tot}. The introduction rates IR were derived from a linear fit and are displayed in the plot.

the light intensity, as well as the competition between electron and hole processes [45,72].

From the data shown in Fig. 5(a), a plot can be constructed displaying the effective trap concentration $N_{t,i}^{eff}$ of the individual defect levels and their dependence on Φ_{tot}. The corresponding results are shown in Fig. 5(b). A linear relationship between Φ_{tot} and $N_{t,i}^{eff}$ is seen for the signatures T_3, T_4, and T_6. However, for T_6, a linear relationship is only seen if one assumes $\Delta C_{illumination}/C_{dark} \approx 0.5$. This is generally a better assumption than assuming $\Delta C_{illumination}/C_{dark} \ll 0.5$ for the junctions studied here. T_1 was not present in this sample. The fact that optically induced emission of electrons as well as holes is relevant for T_5 makes the determination of $N_{t,i}^{eff}$ ambiguous, and hence the corresponding results are not shown here.

The introduction rates IR were derived from a linear fit to $N_{t,i}^{eff}$ versus Φ_{tot}. The following introduction rates were determined for $\Delta C_{illumination}/C_{dark} \ll 0.5$ (average for the cases of neglecting the λ-correction as well as assuming a Franck-Condon shift of up to 1 eV): 6.3×10^4 cm^{-1} (T_3), 1.2×10^5 cm^{-1} (T_4), and 1.5×10^5 cm^{-1} (T_6). For $\Delta C_{illumination}/C_{dark} \approx 0.5$ the following introduction rates IR were computed: 3.3×10^4 cm^{-1} (T_3), 7.5×10^4 cm^{-1} (T_4), and 1.3×10^5 cm^{-1} (T_6). Notably, the derived IR do not differ significantly whether we assume $\Delta C_{illumination}/C_{dark} \ll 0.5$ or $\Delta C_{illumination}/C_{dark} \approx 0.5$. It should be noted that these introduction rates represent a lower bound for the actual introduction rates due to the fact that $N_{t,i}^{eff}$ is always a lower bound for the actual trap concentration $N_{t,i}$ [44,45]. The so-called survival rate can be computed when comparing experimental IR to the expected IR for V_{Ga} and V_O, which was estimated to be 1×10^6 cm^{-1} using SRIM. Using this value, we obtain the following survival rates: 0.03–0.06 (T_3), 0.08–0.12 (T_4), and 0.13–0.15 (T_6) defects per vacancy created.

Figure 6 shows SSPC spectra as well as derivative SSPC spectra recorded on a HVPE-grown Ga_2O_3 thin film before and after implantation with He ions at 120 K. Additionally, results are shown for the sample after He implantation and subsequent exposure to 300 K. The same signatures as seen in Fig. 4 were present in the corresponding Ga_2O_3 thin film before He implantation, with the exception of T_2. After He implantation, T_3 and T_1 are detected, T_4 clearly increases in concentration, while T_6 apparently decreases in concentration. After exposing the sample to 300 K, a significant decrease in the concentration of T_3 and T_4 can be seen, while T_6 seems to increase. The signature labeled T_1 is not affected by the exposure to 300 K. Note that these trends were seen in various samples exposed to similar implantation and annealing

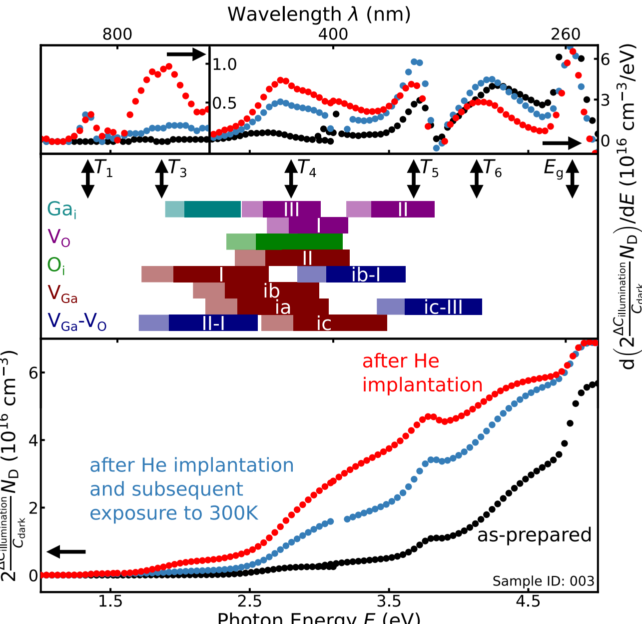

FIG. 6. SSPC spectra recorded on a HVPE-grown Ga_2O_3 thin film before and after He implantation at 120 K with a fluence of 1.25×10^{11} cm^{-2} as well as after a subsequent annealing at 300 K for ~5 min. The results are displayed as derivative SSPC spectra (upper panel) and as conventional SSPC spectra (lower panel). The same signatures as seen in Fig. 4 were present in the corresponding Ga_2O_3 thin film before He implantation, with the exception of T_2. After He implantation, new features labeled T_1 and T_3 are observed, while the signatures T_4 and T_6 change in amplitude. Upon annealing, T_3 and T_4 decrease in amplitude, while T_6 increases in signal. T_1 seems not to be affected by the heat treatment. A panel is also shown with bars representing the computational prediction of optical signatures related to the absorption associated with various primary intrinsic defects as well as divacancy complexes. Results are also shown for the relaxed configurations of V_{Ga}.

conditions (not shown). Figure 6 also shows bars representing the expected position of optical signatures related to the absorption associated with primary intrinsic defects as well as some divacancy complexes. Here, results are also shown for the relaxed configurations of V_{Ga}.

IV. DISCUSSION

On-line SSPC measurements combined with He implantation at cryogenic temperatures (120 K) offer a unique possibility to study the electronic states associated with optically and electrically active primary intrinsic defects, since the diffusion of defects is suppressed. In addition, the migration and/or passivation of defect species mobile at or below room temperature can be studied by subsequent heat treatments, potentially revealing further information about the observed defects. Moreover, we explicitly calculated optical absorption spectra related to the primary intrinsic defects in order to relate signatures seen in SSPC spectra to specific intrinsic defects.

SSPC spectra display several features in as-received HVPE-grown Ga_2O_3 thin films as well as features that are only visible after He implantation at 120 K. The features labeled T_1, T_2, T_3, T_4, and T_6 are steplike, and hence indicate optically induced emission of electrons from trap levels inside the band gap to the conduction band. The feature labeled T_5, on the other hand, is peaklike, and hence clearly displays characteristics of processes related to the optical emission of electrons and holes from a trap level to the conduction band and valence band, respectively [44,45]. However, the electron and hole emission related to T_5 does not have to originate from the same trap. Our results are in accordance with previously reported results, where defect signatures with an onset for optical absorption at around 2.2, 3.2, and 4.4 eV have been measured by SSPC or related techniques [23,24,26,26,27].

Starting with T_1, it is only generated in relatively low concentrations upon He implantation compared to the introduction of the other levels responding to He implantation. In addition, not all samples in the present study display the introduction of T_1 [see Fig. 5(a)]. Interestingly, Farzana *et al.* also observed the introduction of a new defect signature with an onset at around 1.3 eV in SSPC measurements after neutron irradiation [28]. Furthermore, Polyakov *et al.* revealed a level with approximately the same onset energy as T_1 that responded to proton irradiation using CV measurements under illumination [23,24]. The onsets for optical absorption estimated from hybrid-functional calculations corroborate that no primary intrinsic defect exhibits an onset for optical absorption as low as the one observed for T_1. Hence, we propose that T_1 does not arise from a primary intrinsic defect, but rather from a defect complex or an impurity. Further, T_1 is not affected by exposure of the sample to 300 K after He implantation at 120 K, suggesting that T_1 is related to a defect that is not mobile at or below room temperature.

T_5 does not seem to exhibit a pronounced response to He implantation. The same applies to the signature labeled T_2, which is not detected for all samples investigated. This lack of response to He implantation indicates that no primary intrinsic defects are involved, but rather there is an impurity or a defect complex.

For T_3, T_4, and T_6, an approximately linear relationship is seen for their effective trap concentrations in dependence on the accumulated fluence of implanted He ions. Comparing the measured introduction rates with SRIM simulations, the introduced trap concentrations corresponding to T_3, T_4, and T_6 equal about 4%, 10%, and 14% of what is expected for Frenkel-pair generation, respectively. Thus, the IR values for T_3, T_4, and T_6 are close to those expected for primary intrinsic defects.

After implanting He ions at 120 K, one can expect that Ga_i, V_{GaJ} ($J = $ I, II), and V_{OK} ($K = $ I, II, III) will be present, while it is likely that O_i will already have migrated out of the implanted volume and/or formed complexes. Notably, the transformation of V_{GaJ} ($J = $ I, II) into V_{Ga}^{iM} ($M = a, c, b$) is also not expected to occur at 120 K. Even if some defect migration or transformation occurs at 120 K, one can at least expect complex formation to be substantially suppressed.

Comparing the onset of T_3 with the optical absorption of the primary intrinsic defects obtained from the hybrid-functionals calculations, it is evident that the expected onsets for optical absorption computed for $Ga_i^{(+/+2)}$ and $V_{GaI}^{(-3/-2)}$ are close to the position of T_3. Importantly, the optical absorption

expected for V_{GaII}, $V_{\mathrm{O}K}$ (K = I, II, III), and $\mathrm{O_i}$ is located at higher photon energies. The optical signatures related to $V_{\mathrm{GaII}}^{(-3/-2)}$, $V_{\mathrm{O}K}^{(0/+)}$ (K = I, II, III), and $\mathrm{O_i}^{(-2/-)}$ are, however, close to T_4. Thus, $\mathrm{Ga_i}$ and V_{GaI} are potential candidates for T_3, whereas V_{GaII} and $V_{\mathrm{O}K}$ (K = I, II, III) are proposed as candidates for T_4.

However, some of the primary intrinsic defects exhibit several optical charge-state transition levels in the band gap of $\mathrm{Ga_2O_3}$ (see the Supplemental Material [50]). In particular, optical transitions related to $V_{\mathrm{Ga}J}^{(-2/-1)}$ and $V_{\mathrm{Ga}J}^{(-1/0)}$ (J = I, II) may also contribute to T_4. However, the concentration of the defects associated with T_4 is significantly higher than the defect concentration related to T_3, and hence some defects contributing to T_4 are not likely to contribute to T_3.

The exposure of samples implanted with He at cryogenic temperatures to room temperature can further aid the assignment of defect signatures seen in SSPC measurements to specific intrinsic defects. The observed decrease in concentration for T_3 and T_4 upon room-temperature exposure may be explained by annihilation reactions of $\mathrm{Ga_i}$ and V_{Ga} defects. Such annihilation reactions lead to a decrease in $\mathrm{Ga_i}$ as well as $V_{\mathrm{Ga}J}$ (J = I, II), and hence to a decrease of T_3 and T_4. A transformation of $V_{\mathrm{Ga}J}$ (J = I, II) into $V_{\mathrm{Ga}}^{\mathrm{i}M}$ ($M = a, c, b$) should, in contrast, lead to a decrease in the concentration associated with T_3 and an increase in the concentration associated with T_4, taking into account that the transitions related to $V_{\mathrm{Ga}}^{\mathrm{i}M}$ ($M = a, c, b$) are predicted to be close to T_4. However, it is not possible to rule out that both processes, annihilation of $\mathrm{Ga_i}$ with V_{Ga} as well as transformation of V_{Ga}, may contribute to the observed changes in photocapacitance.

Finally, T_6 exhibits an increase in concentration with increasing fluence of He implanted at 120 K, in addition to a distinct increase in concentration after exposure of the samples to room temperature. As mentioned above, several of the intrinsic defects also exhibit charge states in the lower part of the band gap (see the Supplemental Material [50]), and might contribute to T_6. However, the increase in T_6, while T_3 and T_4 decrease, suggests different origins for T_6 compared to T_3 as well as T_4. Hence, it is tempting to propose that T_6 involves a defect complex, rather than a primary intrinsic defect, and divacancies may also be potential candidates for T_6, although the calculated absorption spectra do not result in an adequate fit to the measured position of T_6. Thus, further investigations are required to shed light on the origin of the T_6 level.

V. SUMMARY AND CONCLUSION

Using on-line SSPC measurements, we were able to observe optical transitions related to defects in HVPE-grown $\mathrm{Ga_2O_3}$ thin films with onset energies at 1.3, 1.7, 1.9, 2.6, 3.7, and 4.2 eV. The levels were labeled T_1–T_6 in ascending order of onset energy. T_2, T_4, T_5, and T_6 are observed in all as-received HVPE-grown $\mathrm{Ga_2O_3}$ thin films, whereby T_2 is only observed sporadically. T_1 and T_3 are only detected after He implantation at 120 K. T_4 and T_6 also respond to He implantation. The introduction rates for T_3, T_4, as well as T_6 indicate their relation to primary intrinsic defects. We also calculated migration barriers for $\mathrm{Ga_i}$, and we used reported migration barriers for the vacancy defects [14] and $\mathrm{O_i}$ [15]. Thus, we expect $\mathrm{O_i}$ to be mobile at temperatures below 120 K, and hence to not be present in our samples after He implantation at 120 K. $V_{\mathrm{O}K}$ (K = I, II, III) are not expected to be mobile below room temperature, while $\mathrm{Ga_i}$ should be immobile at 120 K, but be mobile at or below room temperature. $V_{\mathrm{Ga}J}$ (J = I, II) might be mobile just below room temperature, and it is predicted to transform into relaxed configurations that are stable at room temperature [14,19]. We performed hybrid-functional calculations in order to predict the optical absorption cross-section spectra for various primary intrinsic defects. Thus, we tentatively propose T_3 to be associated with $\mathrm{Ga_i}^{(+/+2)}$ and/or $V_{\mathrm{GaI}}^{(-3/-2)}$, whereas T_4 is suggested to be related to $V_{\mathrm{O}K}^{(0/+)}$ (K = I, II, III) and/or $V_{\mathrm{GaII}}^{(-3/-2)}$, although an overlap with other charge-state transitions, such as $V_{\mathrm{Ga}J}^{(-2/-1)}$ and $V_{\mathrm{Ga}J}^{(-1/0)}$ (J = I, II), cannot be excluded.

Further insights were gained by studying the kinetics of the defects created upon He implantation at 120 K. We found that T_3, T_4, and T_6 change in concentration upon exposing samples to room temperature after He implantation at 120 K. T_3 and T_4 decrease in concentration upon such annealing, while T_6 increases in concentration. The kinetics observed for T_3 and T_4 further support the proposed assignments of the corresponding defect signatures to $\mathrm{Ga_i}$ and V_{Ga} due to $\mathrm{Ga_i}$ being mobile already at or below room temperature, and hence annihilation of $\mathrm{Ga_i}$ and V_{Ga} to be a likely mechanism. For T_6, complex formation or passivation involving other defects are proposed to be involved.

ACKNOWLEDGMENTS

Financial support is acknowledged from the Research Council of Norway through the FUNDAMENT project (Project No. 251131), the Norwegian Micro- and Nano-Fabrication Facility (NorFab, Project No. 245963), and the Faculty of Mathematics and Natural Sciences at the University of Oslo via the strategic research initiative FOXHOUND. This work was partially performed under the auspices of the US DOE by Lawrence Livermore National Laboratory under Contract No. DE-AC52-07NA27344, and supported by the Critical Materials Institute, an Energy Innovation Hub funded by the US DOE, Office of Energy Efficiency and Renewable Energy, Advanced Manufacturing Office. We wish to thank Audrius Alkauskas for fruitful collaborations and discussions. We further thank Ole Myren Røhne and Ole Dorholt for wire-bonding of our samples, and Josef Gert Åsheim Ellingsen for proofreading the manuscript.

[1] M. Higashiwaki, K. Sasaki, H. Murakami, Y. Kumagai, A. Koukitu, A. Kuramata, T. Masui, and S. Yamakoshi, Semicond. Sci. Technol. **31**, 034001 (2016).

[2] S. Nakagomi, T. Momo, S. Takahashi, and Y. Kokubun, Appl. Phys. Lett. **103**, 072105 (2013).

[3] S. Nakagomi, T. Sato, Y. Takahashi, and Y. Kokubun, Sens. Actuators A **232**, 208 (2015).
[4] M. A. Mastro, A. Kuramata, J. Calkins, J. Kim, F. Ren, and S. Pearton, ECS J. Solid State Sci. Technol. **6**, P356 (2017).
[5] S. Ahn, Y.-H. Lin, F. Ren, S. Oh, Y. Jung, G. Yang, J. Kim, M. A. Mastro, J. K. Hite, C. R. Eddy Jr. *et al.*, J. Vac. Sci. Technol. B **34**, 041213 (2016).
[6] J. F. McGlone, Z. Xia, Y. Zhang, C. Joishi, S. Lodha, S. Rajan, S. A. Ringel, and A. R. Arehart, IEEE Electron Device Lett. **39**, 1042 (2018).
[7] J. F. McGlone, Z. Xia, C. Joishi, S. Lodha, S. Rajan, S. Ringel, and A. R. Arehart, Appl. Phys. Lett. **115**, 153501 (2019).
[8] J. Lee, S. Ganguli, A. K. Roy, and S. C. Badescu, J. Chem. Phys. **150**, 174706 (2019).
[9] T. Zacherle, P. C. Schmidt, and M. Martin, Phys. Rev. B **87**, 235206 (2013).
[10] S. Lany, APL Mater. **6**, 046103 (2018).
[11] J. R. Ritter, J. Huso, P. T. Dickens, J. B. Varley, K. G. Lynn, and M. D. McCluskey, Appl. Phys. Lett. **113**, 052101 (2018).
[12] J. L. Lyons, Semicond. Sci. Technol. **33**, 05LT02 (2018).
[13] A. Kyrtsos, M. Matsubara, and E. Bellotti, Appl. Phys. Lett. **112**, 032108 (2018).
[14] A. Kyrtsos, M. Matsubara, and E. Bellotti, Phys. Rev. B **95**, 245202 (2017).
[15] M. Ingebrigtsen, A. Y. Kuznetsov, B. Svensson, G. Alfieri, A. Mihaila, U. Badstübner, A. Perron, L. Vines, and J. Varley, APL Mater. **7**, 022510 (2019).
[16] J. Varley, J. Weber, A. Janotti, and C. Van de Walle, Appl. Phys. Lett. **97**, 142106 (2010).
[17] P. Deák, Q. Duy Ho, F. Seemann, B. Aradi, M. Lorke, and T. Frauenheim, Phys. Rev. B **95**, 075208 (2017).
[18] H. J. von Bardeleben, S. Zhou, U. Gerstmann, D. Skachkov, W. R. Lambrecht, Q. D. Ho, and P. Deák, APL Mater. **7**, 022521 (2019).
[19] J. B. Varley, H. Peelaers, A. Janotti, and C. G. Van de Walle, J. Phys.: Condens. Matter **23**, 334212 (2011).
[20] K. Irmscher, Z. Galazka, M. Pietsch, R. Uecker, and R. Fornari, J. Appl. Phys. **110**, 063720 (2011).
[21] M. E. Ingebrigtsen, J. Varley, A. Y. Kuznetsov, B. G. Svensson, G. Alfieri, A. Mihaila, U. Badstübner, and L. Vines, Appl. Phys. Lett. **112**, 042104 (2018).
[22] A. Polyakov, N. Smirnov, I. Shchemerov, E. Yakimov, J. Yang, F. Ren, G. Yang, J. Kim, A. Kuramata, and S. Pearton, Appl. Phys. Lett. **112**, 032107 (2018).
[23] A. Polyakov, N. Smirnov, I. Shchemerov, E. Yakimov, S. Pearton, C. Fares, J. Yang, F. Ren, J. Kim, P. Lagov *et al.*, Appl. Phys. Lett. **113**, 092102 (2018).
[24] A. Polyakov, N. Smirnov, I. Shchemerov, S. Pearton, F. Ren, A. Chernykh, P. Lagov, and T. V. Kulevoy, APL Mater. **6**, 096102 (2018).
[25] A. Polyakov, N. Smirnov, I. Shchemerov, D. Gogova, S. Tarelkin, and S. Pearton, J. Appl. Phys. **123**, 115702 (2018).
[26] E. Farzana, E. Ahmadi, J. S. Speck, A. R. Arehart, and S. A. Ringel, J. Appl. Phys. **123**, 161410 (2018).
[27] Z. Zhang, E. Farzana, A. Arehart, and S. Ringel, Appl. Phys. Lett. **108**, 052105 (2016).
[28] E. Farzana, M. F. Chaiken, T. E. Blue, A. R. Arehart, and S. A. Ringel, APL Mater. **7**, 022502 (2019).
[29] A. Polyakov, N. Smirnov, I. Shchemerov, S. Pearton, F. Ren, A. Chernykh, and A. Kochkova, Appl. Phys. Lett. **113**, 142102 (2018).
[30] Y. Nakano, ECS J. Solid State Sci. Technol. **6**, P615 (2017).
[31] H. Gao, S. Muralidharan, N. Pronin, M. R. Karim, S. M. White, T. Asel, G. Foster, S. Krishnamoorthy, S. Rajan, L. R. Cao *et al.*, Appl. Phys. Lett. **112**, 242102 (2018).
[32] S.-S. Huang, R. Lopez, S. Paul, A. T. Neal, S. Mou, M.-P. Houng, and J. V. Li, Jpn. J. Appl. Phys. **57**, 091101 (2018).
[33] A. T. Neal, S. Mou, S. Rafique, H. Zhao, E. Ahmadi, J. S. Speck, K. T. Stevens, J. D. Blevins, D. B. Thomson, N. Moser *et al.*, Appl. Phys. Lett. **113**, 062101 (2018).
[34] L. Binet and D. Gourier, Appl. Phys. Lett. **77**, 1138 (2000).
[35] G. Schmitz, P. Gassmann, and R. Franchy, J. Appl. Phys. **83**, 2533 (1998).
[36] J. Kim, S. J. Pearton, C. Fares, J. Yang, F. Ren, S. Kim, and A. Y. Polyakov, J. Mater. Chem. C **7**, 10 (2019).
[37] L. Vines, C. Bhoodoo, H. Von Wenckstern, and M. Grundmann, J. Phys.: Condens. Matter **30**, 025502 (2017).
[38] M. A. Blanco, M. B. Sahariah, H. Jiang, A. Costales, and R. Pandey, Phys. Rev. B **72**, 184103 (2005).
[39] P. Weiser, M. Stavola, W. B. Fowler, Y. Qin, and S. Pearton, Appl. Phys. Lett. **112**, 232104 (2018).
[40] C. Bhoodoo, A. Hupfer, L. Vines, E. V. Monakhov, and B. G. Svensson, Phys. Rev. B **94**, 205204 (2016).
[41] A. Hupfer, C. Bhoodoo, L. Vines, and B. G. Svensson, J. Appl. Phys. **119**, 181506 (2016).
[42] J. F. Ziegler, M. D. Ziegler, and J. P. Biersack, Nucl. Instrum. Methods Phys. Res. Sec. B **268**, 1818 (2010).
[43] M. Passlack, N. E. J. Hunt, E. F. Schubert, G. J. Zydzik, M. Hong, J. P. Mannaerts, R. L. Opila, and R. J. Fischer, Appl. Phys. Lett. **64**, 2715 (1994).
[44] P. Blood and J. Orton, *The Electrical Characterization of Semiconductors: Majority Carriers and Electron States*, Techniques of Physics No. 2 (Academic, San Diego, CA, 1992).
[45] A. Chantre, G. Vincent, and D. Bois, Phys. Rev. B **23**, 5335 (1981).
[46] A. White, P. Dean, and P. Porteous, J. Appl. Phys. **47**, 3230 (1976).
[47] T. P. Weiss, A. Redinger, D. Regesch, M. Mousel, and S. Siebentritt, IEEE J. Photovolt. **4**, 1665 (2014).
[48] C. G. Van de Walle and J. Neugebauer, J. Appl. Phys. **95**, 3851 (2004).
[49] A. Alkauskas, M. D. McCluskey, and C. G. Van de Walle, J. Appl. Phys. **119**, 181101 (2016).
[50] See Supplemental Material at http://link.aps.org/supplemental/10.1103/PhysRevMaterials.4.074605 for more information regarding the extraction of trap concentrations from steady-state photocapacitance measurements, and for more information on first-principles calculations of structures, optical charge-state transition levels, and migration barriers of primary intrinsic defects in β-Ga_2O_3, including Refs. [73–76].
[51] P. E. Blöchl, Phys. Rev. B **50**, 17953 (1994).
[52] G. Kresse and D. Joubert, Phys. Rev. B **59**, 1758 (1999).
[53] A. V. Krukau, O. A. Vydrov, A. F. Izmaylov, and G. E. Scuseria, J. Chem. Phys. **125**, 224106 (2006).
[54] G. Kresse and J. Furthmüller, Phys. Rev. B **54**, 11169 (1996).
[55] C. Janowitz, V. Scherer, M. Mohamed, A. Krapf, H. Dwelk, R. Manzke, Z. Galazka, R. Uecker, K. Irmscher, R. Fornari *et al.*, New J. Phys. **13**, 085014 (2011).

[56] T. Onuma, S. Saito, K. Sasaki, K. Goto, T. Masui, T. Yamaguchi, T. Honda, A. Kuramata, and M. Higashiwaki, Appl. Phys. Lett. **108**, 101904 (2016).
[57] C. Freysoldt, B. Grabowski, T. Hickel, J. Neugebauer, G. Kresse, A. Janotti, and C. G. Van de Walle, Rev. Mod. Phys. **86**, 253 (2014).
[58] Y. Kumagai and F. Oba, Phys. Rev. B **89**, 195205 (2014).
[59] C. Freysoldt, J. Neugebauer, and C. G. Van de Walle, Phys. Rev. Lett. **102**, 016402 (2009).
[60] T. Gake, Y. Kumagai, C. Freysoldt, and F. Oba, Phys. Rev. B **101**, 020102(R) (2020).
[61] A. Kopylov and A. Pikhtin, Sov. Phys. Solid State **16**, 1200 (1975).
[62] T. Onuma, S. Saito, K. Sasaki, T. Masui, T. Yamaguchi, T. Honda, and M. Higashiwaki, Jpn. J. Appl. Phys. **54**, 112601 (2015).
[63] H. Peelaers and C. G. Van de Walle, Appl. Phys. Lett. **111**, 182104 (2017).
[64] J. L. Lyons, A. Alkauskas, A. Janotti, and C. G. Van de Walle, Phys. Status Solidi B **252**, 900 (2015).
[65] G. Lucovsky, Solid State Commun. **3**, 299 (1965).
[66] G. Henkelman, B. P. Uberuaga, and H. Jónsson, J. Chem. Phys. **113**, 9901 (2000).
[67] J. P. Perdew, A. Ruzsinszky, G. I. Csonka, O. A. Vydrov, G. E. Scuseria, L. A. Constantin, X. Zhou, and K. Burke, Phys. Rev. Lett. **100**, 136406 (2008).
[68] J. Varley, A. Janotti, C. Franchini, and C. G. Van de Walle, Phys. Rev. B **85**, 081109(R) (2012).
[69] B. E. Kananen, N. C. Giles, L. E. Halliburton, G. K. Foundos, K. B. Chang, and K. Stevens, J. Appl. Phys. **122**, 215703 (2017).
[70] K. H. Warnick, Y. Puzyrev, T. Roy, D. M. Fleetwood, R. D. Schrimpf, and S. T. Pantelides, Phys. Rev. B **84**, 214109 (2011).
[71] M. Schubert, R. Korlacki, S. Knight, T. Hofmann, S. Schöche, V. Darakchieva, E. Janzén, B. Monemar, D. Gogova, Q.-T. Thieu, R. Togashi, H. Murakami, Y. Kumagai, K. Goto, A. Kuramata, S. Yamakoshi, and M. Higashiwaki, Phys. Rev. B **93**, 125209 (2016).
[72] Y. Furukawa, Jpn. J. Appl. Phys. **6**, 675 (1967).
[73] B. Monemar and L. Samuelson, Phys. Rev. B **18**, 809 (1978).
[74] T. Takebe, J. Saraie, and H. Matsunami, J. Appl. Phys. **53**, 457 (1982).
[75] R. Pässler, J. Appl. Phys. **96**, 715 (2004).
[76] D. Wickramaratne, C. E. Dreyer, B. Monserrat, J.-X. Shen, J. L. Lyons, A. Alkauskas, and C. G. Van de Walle, Appl. Phys. Lett. **113**, 192106 (2018).